Strategic Damping Placement in Viscoelastic Bandgap Structures: **Dissecting the Metadamping** Phenomenon in Multiresonator **Metamaterials**

A. Aladwani

Department of Manufacturing Engineering Technology, College of Technological Studies, Shuwaikh 70654, Kuwait e-mail: ae.aladwani@paaet.edu.kw

M. Nouh

Department of Mechanical and Aerospace Engineering, University at Buffalo (SUNY), Buffalo, NY 14260, e-mail: mnouh@buffalo.edu

Energy dissipation in polymeric composite metamaterials requires special mathematical models owing to the viscoelastic nature of their constituents, namely, the polymeric matrix, bonding agent, and local resonators. Unlike traditional composites, viscoelastic metamaterials possess a unique ability to exhibit strong wave attenuation while retaining high stiffness as a result of the "metadamping" phenomenon attributed to local resonances. The objective of this work is to investigate viscoelastic metadamping in one-dimensional multibandgap metamaterials by combining the linear hereditary theory of viscoelasticity with the Floquet-Bloch theory of wave propagation in infinite elastic media. Important distinctions between metamaterial and phononic unit cell models are explained based on the free wave approach with wavenumber-eliminated damping-frequency band structures. The developed model enables viscoelastic metadamping to be investigated by varying two independent relaxation parameters describing the viscoelasticity level in the host structure and the integrated resonators. The dispersion mechanics within high damping regimes and the effects of boundary conditions on the damped response are detailed. The results reveal that in a multiresonator cell, strategic damping placement in the individual resonators plays a profound role in shaping intermediate dispersion branches and dictating the primary and secondary frequency regions of interest, within which attenuation is most required. [DOI: 10.1115/1.4048802]

Keywords: elastic metamaterial, metadamping, viscoelasticity, bandgap, vibration, wave propagation

> with and alters their dispersion mechanics and dynamic response. More importantly, owing to natural trends and coupling of mechan-

> ical properties (often depicted in Ashby charts of commonly avail-

able materials), high dissipation levels are usually associated with

softer materials, posing serious questions about their ability to func-

tion in certain environments and heavy applications. Over the past

decade, LRMs—where the interplay between a host structure and

periodic resonant inclusions instigates subwavelength and size-

independent bandgaps—have jumped to the forefront of material

candidates that can be tailored to exhibit strong attenuation while

retaining high stiffness. The ability of LRMs to provide this

elusive combination stems from the concept of "damping emer-

gence," i.e., the ability of an internal structure of a material to

whip up its dissipation performance compared to other materials

with the same damping composition and equivalent static properties.

The latter notion is often referred to as *metadamping*, a term coined

by Hussein and Frazier who first conceptualized this problem in

canonical spring-mass lattices [20]. The phenomenon has since

spurted a number of efforts, which have examined metadamping in

the context of viscoelastic metamaterials [21], nontraditional crystals

[22], flexural systems [23], as well as fractional calculus [24]. Exper-

imental evidence of positive and negative metadamping (i.e.,

enhanced and reduced dissipation) in continuous flexural systems

1 Introduction

The study of periodic systems has recently matured and evolved into a research field that offers a versatile platform for the synthesis of mechanical structures with properties that go beyond traditional and natural limits [1]. Specifically, in the domain of acoustic and elastic wave propagation, periodic architectures such as phononic crystals (PCs) and locally resonant metamaterials (LRMs) have been shown to harbor unique and unprecedented wave dispersion characteristics, which culminate in frequency bandgaps, i.e., extended ranges of forbidden wave propagation, as well as interesting directional filtering and energy guidance capabilities [2-6]. Most recently, the tailoring of such PCs and LRMs, and variations thereof, via active inserts [7,8], topology optimization [9], symmetry breakage [10], fluid-coupling [11], or selective control of material properties in time and space [12] have given rise to unconventional patterns related to insulation [13], atomic and nanoscale heat transfer [14,15], and wave reciprocity [16,17], which uniquely position such periodic systems to fundamentally alter and transform a wide range of vibroacoustic engineering applications.

Although the hallmark features of PCs and LRMs (e.g., frequency bandgaps) take place in the nondissipative form of such systems, the effect of damping cannot be ignored [18,19]. Practically speaking, almost all composite and composite-like structures exhibit a certain degree of viscous or viscoelastic damping, which interferes

was recently presented [25]. A comprehensive overview of metadamping in elastic metamaterials can be found in the study by Bacquet et al. [26]. Fiber-reinforced polymers (FRPs) are a class of composite mate-

rials characterized by high stiffness and strength, low density, as well as tunable damping properties that differ from traditional engineering materials. The driving mechanism of energy dissipation in FRPs stems from the polymeric matrix and bonding agents that

¹Corresponding author.

Contributed by the Applied Mechanics Division of ASME for publication in the JOURNAL OF APPLIED MECHANICS. Manuscript received August 5, 2020; final manuscript received October 14, 2020; published online November 3, 2020. Assoc. Editor: Shao-

exhibit viscoelastic features. By increasing the volume fraction of the matrix and/or bonding agents, damping will increase at the expense of stiffness and strength. Thermosets (such as epoxy) are generally preferred over thermoplastics because they exhibit higher stiffness and better adhesion properties balanced with eminent (yet lower) damping characteristics [27,28]. Although considered the main contributor to damping, the matrix is not the only source of energy dissipation in composite materials. Several other sources include [29,30] (1) damping in the fibers, (2) damping due to interphase, (3) damping due to damage, (4) thermoelastic damping, and (5) viscoplastic damping. The current literature contains numerous methods for predicting composite damping, ranging from analytical and computational models [31-34] to experimental characterization techniques [35-38]. When FRP is augmented with viscoelastic resonant inclusions, the resultant viscoelastic metamaterial attains superior attenuation levels combined with a high strength-to-mass ratio. The effects of dissipation in viscoelastic metamaterials have been studied, for example, using Kelvin-Voigt and generalized Maxwell models [39] and in the context of the dynamic homogenization theory [40].

Motivated by the previous expectations and the fact that LRMs can operate efficiently only within stringent damping limits or constraints, this article is concerned with the modeling and analysis of the metadamping phenomenon associated with multiresonator viscoelastic metamaterials. To this end, the free wave approach is used to investigate the dispersion mechanics of a graphite-epoxy metamaterial beam both in the infinite and finite medium configurations. This article is organized as follows: following Sec. 1, the finite element formulation for computing viscoelastic band structures is detailed along with numerical validations against commonly used viscously damped models. Section 3, which constitutes the greater part of this effort, focuses on elucidating the metadamping phenomenon encountered in the damping-frequency band structures across independent configurations of one-dimensional (1D) composites comprising two viscoelastic resonators. Within the analyses, the mechanics of dispersion in high damping regimes and the effects of physical boundary conditions on the beam's damped response are discussed. The obtained results will then be generalized for composite metamaterials with multiple resonators. Finally, the conclusions of the current work are summarized.

2 Viscoelastic Band Structure Computation

We start by presenting a comprehensive mathematical framework for computing damped band structures (also known as dispersion diagrams) of viscoelastic and viscous 1D periodic structures based on the free wave approach. Within the analysis, important distinctions between (1) metamaterial and (2) phononic unit cell models are explained in details.

2.1 Viscous Damping Model. Consider a free unit cell of a 1D infinitely periodic structure with a displacement field denoted by the vector **u**. According to Bloch's theorem, such wave field vector can be expressed as follows:

$$\mathbf{u}(x, \kappa, t) = \tilde{\mathbf{u}}(x, \kappa)e^{j\kappa x + \lambda t} \tag{1}$$

satisfying the periodicity constraint $\tilde{\mathbf{u}}(x, \kappa, t) = \tilde{\mathbf{u}}(x + a, \kappa, t)$, where $\tilde{\mathbf{u}}$ is the periodic amplitude vector, a represents the spatial periodicity of the unit cell in the x-direction, κ is the wavenumber, and λ is a complex frequency function that permits wave attenuation in time. Applying the periodicity constraint, Eq. (1) can be rewritten as a relationship between the unit cell boundaries such that

$$\mathbf{u}(x+a,\kappa,t) = \mathbf{u}(x,\kappa,t)e^{j\kappa a} \tag{2}$$

In the context of the finite element method (FEM), \mathbf{u} is discretized into generalized displacements satisfying the motion equations given by $\mathbf{M}\ddot{\mathbf{U}} + \mathbf{D}\dot{\mathbf{U}} + \mathbf{K}\mathbf{U} = \mathbf{0}$, where \mathbf{U} is the free generalized displacements vector and \mathbf{M} , \mathbf{D} , and \mathbf{K} denote the unit cell mass,

viscous damping, and stiffness matrices, respectively. For discretized models, Eq. (2) is equivalent to a set of equations relating the generalized displacements of the unit cells' right boundary to their left counterparts. This implies that $\mathbf{U} = \begin{bmatrix} \mathbf{U}_L & \mathbf{U}_I & \mathbf{U}_R \end{bmatrix}^T$, which contains the full set of rearranged degrees-of-freedom (DOFs), can be expressed as $\mathbf{U} = \mathbf{P}\tilde{\mathbf{U}}$, where $\tilde{\mathbf{U}} = \begin{bmatrix} \mathbf{U}_L & \mathbf{U}_I \end{bmatrix}^T$ is the periodic generalized displacements vector that contains the minimal set of DOFs (including only internal and left boundary displacements and rotations), and \mathbf{P} is the Bloch periodicity matrix, which is expressed as follows:

$$\mathbf{P}(\kappa) = \begin{bmatrix} \mathbf{I} & \mathbf{0} \\ \mathbf{0} & \mathbf{I} \\ \mathbf{0} & \mathbf{I}e^{j\kappa a} \end{bmatrix}$$
(3)

where I and $\mathbf{0}$ are identity and null matrices of proper sizes, respectively. Consequently, unit cell equations can be written in terms of $\tilde{\mathbf{U}}$ as follows:

$$\tilde{\mathbf{M}}\ddot{\tilde{\mathbf{U}}} + \tilde{\mathbf{D}}\dot{\tilde{\mathbf{U}}} + \tilde{\mathbf{K}}\tilde{\mathbf{U}} = \mathbf{0} \tag{4}$$

where the reduced matrices $\tilde{\mathbf{M}}$, $\tilde{\mathbf{D}}$, and $\tilde{\mathbf{K}}$ can be computed via

$$\tilde{\mathbf{M}} = \mathbf{P}^{\dagger} \mathbf{M} \mathbf{P} \tag{5a}$$

$$\tilde{\mathbf{D}} = \mathbf{P}^{\dagger} \mathbf{D} \mathbf{P} \tag{5b}$$

$$\tilde{\mathbf{K}} = \mathbf{P}^{\dagger} \mathbf{K} \mathbf{P} \tag{5c}$$

where \mathbf{P}^{\dagger} being the Hermitian transpose of the Bloch periodicity matrix. Equation (4) can be recast into a state-space transformation by introducing the state vector $\tilde{\mathbf{Y}} = [\dot{\tilde{\mathbf{U}}} \quad \tilde{\mathbf{U}}]^T$, yielding

$$\tilde{\mathbf{A}}\dot{\tilde{\mathbf{Y}}} + \tilde{\mathbf{B}}\tilde{\mathbf{Y}} = \mathbf{0} \tag{6}$$

where

$$\tilde{A} = \begin{bmatrix} 0 & \tilde{M} \\ \tilde{M} & \tilde{D} \end{bmatrix} \quad \text{and} \quad \tilde{B} = \begin{bmatrix} -\tilde{M} & 0 \\ 0 & \tilde{K} \end{bmatrix} \tag{7}$$

From Eq. (6), the following linear eigenvalue problem

$$(\lambda \tilde{\mathbf{A}} + \tilde{\mathbf{B}})\bar{\mathbf{Y}} = \mathbf{0} \tag{8}$$

is obtained by assuming a solution $\tilde{\mathbf{Y}} = \bar{\mathbf{Y}}e^{\lambda t}$, which yields complex eigenvalues of the form $\lambda(\kappa) = -\zeta_d(\kappa)\omega_r(\kappa) \pm j\omega_d(\kappa)$, where

$$\omega_d(\kappa) = \operatorname{Im}[\lambda(\kappa)] \quad \text{and} \quad \zeta_d(\kappa) = -\frac{\operatorname{Re}[\lambda(\kappa)]}{|\lambda(\kappa)|}$$
 (9)

where ω_r , ω_d , and ζ_d are the wavenumber-dependent undamped frequency, damped frequency, and damping ratio, respectively. While this research effort is primarily concerned with the analysis of viscoelastic dissipation, the above formulation for viscous wave propagation is included as a benchmark against which the viscoelastic behavior will be evaluated as outlined in Sec. 2.3.

2.2 Viscoelastic Damping Model. For a viscoelastic material, damping behavior is classically modeled using the linear hereditary theory where the nonviscous damping forces depend on the history of generalized velocities via convolution integrals over kernel functions [41]. In this case, the motion of a free unit cell representing an infinitely periodic viscoelastic medium can be generally described by integro-differential equations of the form:

$$\tilde{\mathbf{M}}\ddot{\tilde{\mathbf{U}}}(t) + \int_{0}^{t} \mathbf{G}(t-\tau)\dot{\tilde{\mathbf{U}}}(\tau)d\tau + \tilde{\mathbf{K}}\tilde{\mathbf{U}}(t) = \mathbf{0}$$
 (10)

where $G(t-\tau)$ is a matrix of damping kernel functions (also known as hereditary functions) with a series of parameters that are typically

Table 1 Some viscoelastic functions in the Laplace domain [45]

Viscoelastic function	Ref.
$G(s) = \sum_{k=1}^{n} \frac{a_k}{s + b_k}$	[46]

$$G(s) = G^{\infty} \left[\sum_{k=1}^{n} \alpha_k \frac{s + 2\zeta_k \omega_k}{s^2 + 2\zeta_k \omega_k s + \omega_k^2} \right]$$
 [42,47]

$$G(s) = 1 + \sum_{k=1}^{n} \frac{\Delta_k s}{s + \beta_k}$$
 [48]

identified on master curves. Many viscoelastic models have been developed and applied to replicate the frequency-dependent viscoelastic material properties including, but not limited to, the Golla–Hughes–McTavish [42], the anelastic displacement field [43], and the exponential damping models [44]. Some of the kernel functions commonly known in the literature are presented in Table 1. In this article, the exponential damping model is implemented due to its mathematical convenience for modeling complex viscoelastic structures incorporating combination of damping mechanisms arising from the host structure and/or local resonators. The model also enables us to tune the relaxation parameters as needed to replicate the behavior of (a) a purely elastic material, (b) a purely viscous material, or (c) a viscoelastic material that provides a critical validation mechanism of the results presented here.

The exponential damping model is associated with a matrix of damping kernel functions of the following form:

$$\mathbf{G}(t) = \sum_{k=1}^{n} \mu_k e^{-\mu_k t} \tilde{\mathbf{D}}_k$$
 (11)

where μ_k are known as the relaxation parameters and n is the number of parameters required to replicate the damping behavior of a given viscoelastic material. Substituting Eq. (11) into (10) yields

$$\tilde{\mathbf{M}}\ddot{\tilde{\mathbf{U}}}(t) + \sum_{k=1}^{n} \tilde{\mathbf{D}}_{k} \left[\int_{0}^{t} \mu_{k} e^{-\mu_{k}(t-\tau)} \dot{\tilde{\mathbf{U}}}(\tau) d\tau \right] + \tilde{\mathbf{K}}\tilde{\mathbf{U}}(t) = \mathbf{0}$$
 (12)

First, we introduce a set of internal variables $\tilde{\mathbf{Z}}_k$, such that

$$\tilde{\mathbf{Z}}_{k}(t) = \int_{0}^{t} \mu_{k} e^{-\mu_{k}(t-\tau)} \dot{\tilde{\mathbf{U}}}(\tau) d\tau$$
 (13)

$$\tilde{\mathbf{M}}\ddot{\tilde{\mathbf{U}}}(t) + \sum_{k=1}^{n} \tilde{\mathbf{D}}_{k} \tilde{\mathbf{Z}}_{k}(t) + \tilde{\mathbf{K}}\tilde{\mathbf{U}}(t) = \mathbf{0}$$
(14)

Second, Eq. (13) is differentiated with respect to time, and the Leibniz's integral rule is applied to the right-hand side of the equation, yielding

$$\dot{\tilde{\mathbf{Z}}}_{k}(t) = -\int_{0}^{t} \mu_{k}^{2} e^{-\mu_{k}(t-\tau)} \dot{\tilde{\mathbf{U}}}(\tau) d\tau + \mu_{k} \dot{\tilde{\mathbf{U}}}(t) = \mu_{k} \left[\dot{\tilde{\mathbf{U}}}(t) - \tilde{\mathbf{Z}}_{k}(t) \right]$$
(15)

Premultiplying Eq. (15) by $\tilde{\mathbf{D}}_k$ and dividing by μ_k^2 leads to the following viscoelastic dynamical equations of motion:

$$\tilde{\mathbf{M}}\ddot{\tilde{\mathbf{U}}} + \sum_{k=1}^{n} \tilde{\mathbf{D}}_{k} \left[\dot{\tilde{\mathbf{U}}} - \frac{1}{\mu_{k}} \dot{\tilde{\mathbf{Z}}}_{k} \right] + \tilde{\mathbf{K}}\tilde{\mathbf{U}} = \mathbf{0}$$
 (16a)

$$-\frac{1}{\mu_k}\tilde{\mathbf{D}}_k\dot{\tilde{\mathbf{U}}} + \frac{1}{\mu_k^2}\tilde{\mathbf{D}}_k\dot{\tilde{\mathbf{Z}}}_k = -\frac{1}{\mu_k}\tilde{\mathbf{D}}_k\tilde{\mathbf{Z}}_k$$
(16b)

To formulate a state-space problem equivalent to Eq. (6), we define a new state vector $\tilde{\mathbf{Y}} = \begin{bmatrix} \dot{\tilde{\mathbf{U}}} & \tilde{\mathbf{U}} & \tilde{\mathbf{Z}}_1 & \tilde{\mathbf{Z}}_2 & \cdots & \tilde{\mathbf{Z}}_n \end{bmatrix}^T$, which leads to the following matrices:

$$\tilde{\mathbf{A}} = \begin{bmatrix} \mathbf{0} & \tilde{\mathbf{M}} & \mathbf{0} & \mathbf{0} & \cdots & \mathbf{0} \\ \tilde{\mathbf{M}} & \sum_{k=1}^{n} \tilde{\mathbf{D}}_{k} & \frac{-1}{\mu_{1}} \tilde{\mathbf{D}}_{1} & \frac{-1}{\mu_{2}} \tilde{\mathbf{D}}_{2} & \cdots & \frac{-1}{\mu_{n}} \tilde{\mathbf{D}}_{n} \\ \mathbf{0} & \frac{-1}{\mu_{1}} \tilde{\mathbf{D}}_{1} & \frac{1}{\mu_{1}^{2}} \tilde{\mathbf{D}}_{1} & \mathbf{0} & \cdots & \mathbf{0} \\ \mathbf{0} & \frac{-1}{\mu_{2}} \tilde{\mathbf{D}}_{2} & \mathbf{0} & \frac{1}{\mu_{2}^{2}} \tilde{\mathbf{D}}_{2} & \cdots & \mathbf{0} \\ \vdots & \vdots & \vdots & \vdots & \ddots & \vdots \\ \mathbf{0} & \frac{-1}{\mu_{n}} \tilde{\mathbf{D}}_{n} & \mathbf{0} & \mathbf{0} & \cdots & \frac{1}{\mu_{n}^{2}} \tilde{\mathbf{D}}_{n} \end{bmatrix}$$

$$(17a)$$

$$\tilde{\mathbf{B}} = \operatorname{diag} \left[-\tilde{\mathbf{M}} \quad \tilde{\mathbf{K}} \quad \frac{1}{\mu_1} \tilde{\mathbf{D}}_1 \quad \frac{1}{\mu_2} \tilde{\mathbf{D}}_2 \quad \cdots \quad \frac{1}{\mu_n} \tilde{\mathbf{D}}_n \right]$$
(17b)

where diag[] contains the elements of a block diagonal matrix. For a phononic unit cell, the matrices given in Eq. (17) are sufficient to formulate an eigenvalue problem equivalent to the one provided by Eq. (8) since for this particular case, all $\tilde{\mathbf{D}}_k$ matrices are of full rank. On the opposite hand, a metamaterial unit cell may, under certain circumstances, produce $\tilde{\mathbf{D}}_k$ matrices that are rank deficient, which requires further manipulations before solving its associated

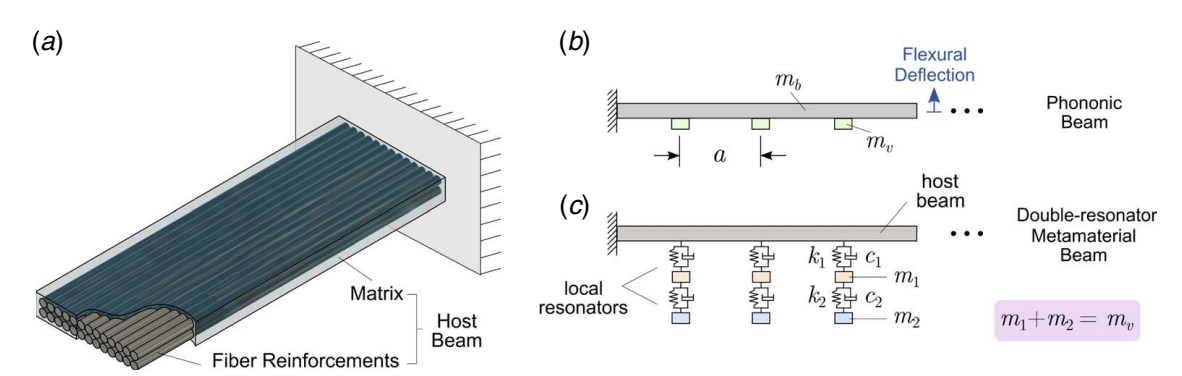


Fig. 1 Schematic diagram of (a) A cantilevered fiber-reinforced composite beam along with two distinct periodic configurations: (b) A phononic beam and (c) A double-resonator metamaterial beam with local resonators connected in series. The unit cells in both cases are a distance a apart.

eigenvalue problem. For each rank deficient $\tilde{\mathbf{D}}_k$, we define the partitioning $\mathbf{\Phi}_k = \begin{bmatrix} \mathbf{\Phi}_{kp} & \mathbf{\Phi}_{ks} \end{bmatrix}$, where the columns of $\mathbf{\Phi}_{kp}$ and $\mathbf{\Phi}_{ks}$ are the eigenvectors corresponding to nonzero (p) and zero (s) eigenvalues of $\tilde{\mathbf{D}}_k$, respectively. A reduced set of internal variables $\tilde{\mathbf{Z}}_k^r$ is then introduced, such that $\tilde{\mathbf{Z}}_k = \mathbf{\Phi}_{kp} \tilde{\mathbf{Z}}_k^r$. Upon substituting the previous relation into Eq. (16) and premultiplying Eq. (16b) by $\mathbf{\Phi}_{kp}^T$, we arrive at

$$\tilde{\mathbf{M}}\ddot{\tilde{\mathbf{U}}} + \sum_{k=1}^{n} \tilde{\mathbf{D}}_{k} \left[\dot{\tilde{\mathbf{U}}} - \frac{1}{\mu_{k}} \mathbf{\Phi}_{kp} \dot{\tilde{\mathbf{Z}}}_{k}^{r} \right] + \tilde{\mathbf{K}}\tilde{\mathbf{U}} = \mathbf{0}$$
 (18*a*)

$$-\frac{1}{\mu_k} \mathbf{\Phi}_{kp}^T \tilde{\mathbf{D}}_k \dot{\tilde{\mathbf{U}}} + \frac{1}{\mu_k^2} \mathbf{\Phi}_{kp}^T \tilde{\mathbf{D}}_k \mathbf{\Phi}_{kp} \dot{\tilde{\mathbf{Z}}}_k^r = -\frac{1}{\mu_k} \mathbf{\Phi}_{kp}^T \tilde{\mathbf{D}}_k \mathbf{\Phi}_{kp} \tilde{\mathbf{Z}}_k^r \qquad (18b)$$

Finally, a reduced state vector $\tilde{\mathbf{Y}}^r = \begin{bmatrix} \dot{\mathbf{U}} & \tilde{\mathbf{U}} & \tilde{\mathbf{Z}}_1^r & \tilde{\mathbf{Z}}_2^r & \cdots & \tilde{\mathbf{Z}}_p^r \end{bmatrix}^T$ is defined, which allows Eqs. (18a) and (18b) to be combined into the reduced state-space form given by

$$\tilde{\mathbf{A}}^r \dot{\tilde{\mathbf{Y}}}^r + \tilde{\mathbf{B}}^r \tilde{\mathbf{Y}}^r = \mathbf{0} \tag{19}$$

where

$$\tilde{\mathbf{A}}^{r} = \begin{bmatrix} \mathbf{0} & \tilde{\mathbf{M}} & \mathbf{0} & \mathbf{0} & \cdots & \mathbf{0} \\ \tilde{\mathbf{M}} & \sum_{k=1}^{n} \tilde{\mathbf{D}}_{k} & \frac{-1}{\mu_{1}} \tilde{\mathbf{D}}_{1} \mathbf{\Phi}_{1p} & \frac{-1}{\mu_{2}} \tilde{\mathbf{D}}_{2} \mathbf{\Phi}_{2p} & \cdots & \frac{-1}{\mu_{n}} \tilde{\mathbf{D}}_{n} \mathbf{\Phi}_{np} \\ \mathbf{0} & \frac{-1}{\mu_{1}} \mathbf{\Phi}_{1p}^{T} \tilde{\mathbf{D}}_{1} & \frac{1}{\mu_{1}^{2}} \mathbf{\Phi}_{1p}^{T} \tilde{\mathbf{D}}_{1} \mathbf{\Phi}_{1p} & \mathbf{0} & \cdots & \mathbf{0} \\ \mathbf{0} & \frac{-1}{\mu_{2}} \mathbf{\Phi}_{2p}^{T} \tilde{\mathbf{D}}_{2} & \mathbf{0} & \frac{1}{\mu_{2}^{2}} \mathbf{\Phi}_{2p}^{T} \tilde{\mathbf{D}}_{2} \mathbf{\Phi}_{2p} & \cdots & \mathbf{0} \\ \vdots & \vdots & \vdots & \vdots & \ddots & \vdots \\ \mathbf{0} & \frac{-1}{\mu_{n}} \mathbf{\Phi}_{np}^{T} \tilde{\mathbf{D}}_{n} & \mathbf{0} & \mathbf{0} & \cdots & \frac{1}{\mu_{n}^{2}} \mathbf{\Phi}_{np}^{T} \tilde{\mathbf{D}}_{n} \mathbf{\Phi}_{np} \end{bmatrix}$$
(20a)

$$\tilde{\mathbf{B}}^r = \operatorname{diag} \left[-\tilde{\mathbf{M}} \quad \tilde{\mathbf{K}} \quad \frac{1}{\mu_1} \mathbf{\Phi}_{1p}^T \tilde{\mathbf{D}}_1 \mathbf{\Phi}_{1p} \quad \frac{1}{\mu_2} \mathbf{\Phi}_{2p}^T \tilde{\mathbf{D}}_2 \mathbf{\Phi}_{2p} \quad \cdots \quad \frac{1}{\mu_n} \mathbf{\Phi}_{np}^T \tilde{\mathbf{D}}_n \mathbf{\Phi}_{np} \right]$$
(20b)

From Eqs. (17) and (20), it can be observed that in the limit $\mu_k \to \infty \, \forall k$, the viscous state-space form given in Eq. (7) is recovered. The previous implies that high values of μ_k yield a viscous-like behavior that is less dependent on the history, while low values of μ_k are more representative of a full-fledged viscoelastic behavior.

2.3 Numerical Validations. Before pursuing an investigation of viscoelastic metadamping, which is a phenomenon associated

with dissipative metamaterials, an initial set of results produced from the analysis of viscoelastic phononic materials is briefly outlined here as a baseline for future comparisons. Moreover, this step provides a simple way for validating the viscoelastic model presented in Sec. 2.2. To this end, let us consider a 1D fiber-reinforced composite structure as shown in Fig. 1(a). It consists of a 3 mm thick, 40 mm wide, and 360 mm long [0 deg] graphite-epoxy cantilever beam with the following material properties [49]: $\rho = 1389.23 \text{ kg/m}^3$, $E_1 = 144.80 \text{ GPa}$, $E_2 = 9.65 \text{ GPa}$,

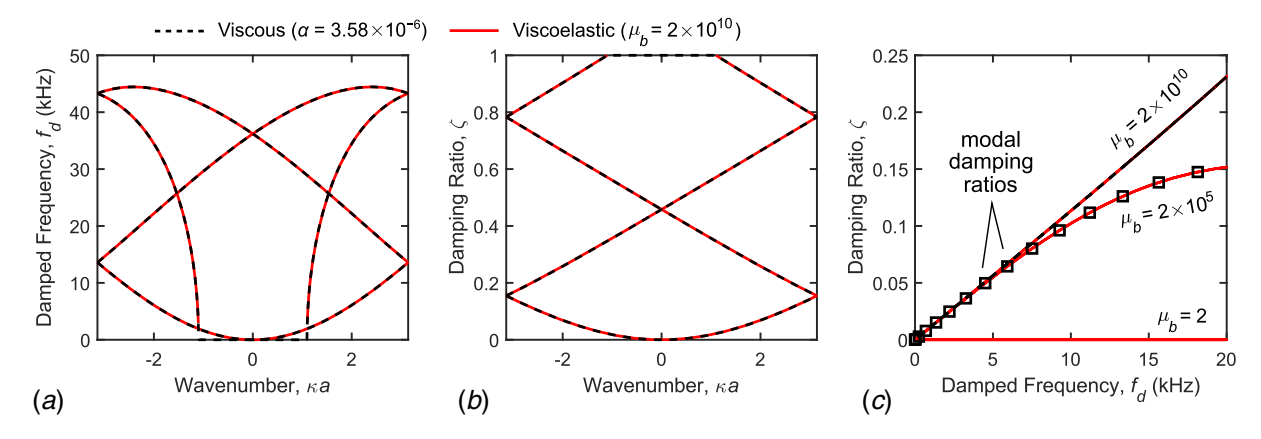


Fig. 2 (a) Frequency and (b) damping ratio band structures for a unit cell of the plain composite beam using the viscoelastic (red, solid) and viscous (black, dotted) damping models when $\mu_b = 2 \times 10^{10}$. (c) Damping-frequency band structure using relaxation parameters that are tuned to three different damping regimes: (1) undamped, $\mu_b = 2$, (2) viscoelastic, $\mu_b = 2 \times 10^5$, and (3) viscous, $\mu_b = 2 \times 10^{10}$. Modal damping ratios of the finite beam corresponding to $\mu_b = 2 \times 10^5$ are shown in (c) as discrete squares.

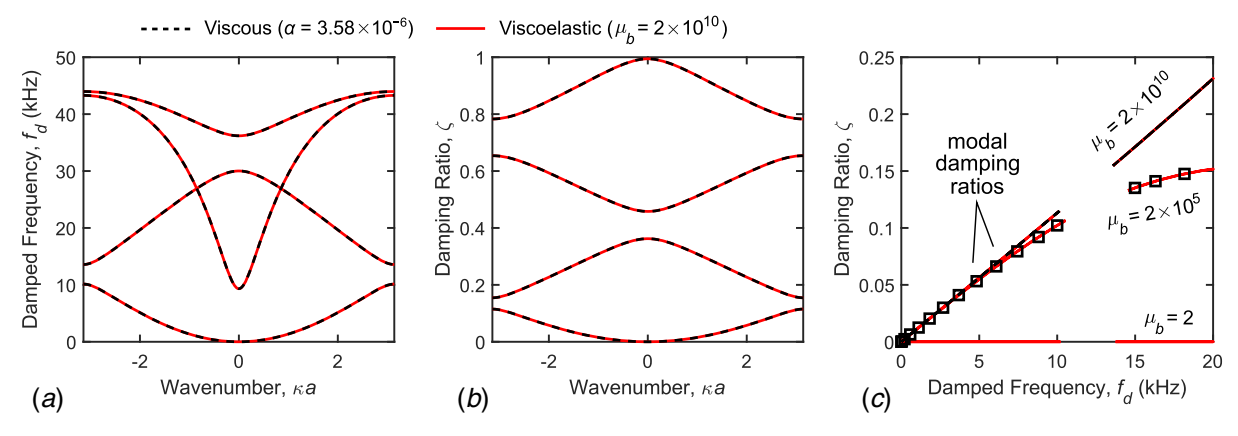


Fig. 3 (a) Frequency and (b) damping ratio band structures for a unit cell of the phononic composite beam using the viscoelastic (red, solid) and viscous (black, dotted) damping models when $\mu_b = 2 \times 10^{10}$. (c) Damping-frequency band structure using relaxation parameters that are tuned to three different damping regimes: (1) undamped, $\mu_b = 2$, (2) viscoelastic, $\mu_b = 2 \times 10^5$, and (3) viscous, $\mu_b = 2 \times 10^{10}$. Modal damping ratios of the finite beam corresponding to $\mu_b = 2 \times 10^5$ are shown in (c) as discrete squares.

 $G_{12} = G_{13} = 4.14 \text{ GPa}, G_{23} = 3.45 \text{ GPa}, \text{ and } \nu_{12} = 0.3, \text{ where } \rho, E, G,$ and ν denote the density, elastic modulus, shear modulus, and Poisson's ratio along the different directions, respectively. A series of 12 lumped masses are periodically attached to the lower surface of the composite beam at equally spaced distances a = 30 mm, as shown in Fig. 1(b). The lumped masses are chosen such that $m_v = 0.4 m_b$, where m_v and m_b denote the lumped and beam masses in a single-unit cell. A notable advantage of the viscoelastic model presented in Sec. 2.2 is its ability to be validated against classical viscous damping models. The previous hypothesis can be validated by assuming that $\mathbf{D}_b = \alpha \mathbf{K}_b$, where \mathbf{D}_b and \mathbf{K}_b represent the viscous damping and stiffness matrices, respectively, associated with the composite beam and α is a proportionality constant. Throughout this study, the FEM used to obtain unit cell predictions is based on the first shear deformation theory and Timoshenko beam assumptions (see Ref. [50] for details). Furthermore, while fiber orientation plays a significant role in dictating several mechanical properties of a given composite material, its effect on energy dissipation is beyond the scope of this effort. Alternatively, a single relaxation parameter μ_b will be used to describe the damping behavior of the considered unidirectional composite beam, enabling the metadamping phenomenon to be evaluated in a general sense rather than the behavior of a particular viscoelastic material. As such, it becomes plausible to tune the beam's viscoelasticity level (dependence on the history) to one of three damping regimes, namely, (1) undamped, (2) viscoelastic, or (3) viscous [21].

In Figs. 2(a) and 2(b), frequency and damping ratio band structures are shown for viscous ($\alpha = 3.58 \times 10^{-6}$) and viscoelastic (μ_b $=2\times10^{10}$) plain composite beams (in the absence of lumped masses). For such a large value of μ_b , it can be observed that the band structures of both beams are almost identical across the entire wavenumber spectrum. To clearly demonstrate the effects of viscoelasticity on the mechanics of dispersion, Fig. 2(c) is constructed from a combination of Figs. 2(a) and 2(b). The main advantage of the resulting figure (henceforth denoted as the damping-frequency band structure) stems from its readability convenience since it eliminates the wavenumber completely, providing a direct correlation between Bloch damping ratios and the associated oscillatory frequencies. The damping-frequency band structure is computed for three different μ_b values. The first value is selected to be $\mu_b = 2$, which is small enough to replicate the behavior of an undamped beam, producing substantially small values of Bloch damping ratios across the entire frequency spectrum as inferred from the flat line coinciding with the frequency axis. For $\mu_b = 2 \times$ 10^{10} , which was used to construct Figs. 2(a) and 2(b), the viscous damping case is recovered, hence validating the proposed viscoelastic model for the case of a plain composite beam. The figure also depicts an additional intermediate curve representing a more realistic behavior of a viscoelastic beam with $\mu_b = 2 \times 10^5$. For this particular case, modal damping ratios of the corresponding finite cantilever beam are plotted as discrete points in the same figure and showing excellent agreement with the Bloch damping ratios in the considered frequency range (0–20 kHz).

In a second validation step, the same parameters ($\alpha = 3.58 \times 10^{-6}$ and $\mu_b = 2 \times 10^{10}$) are used to construct the frequency and the damping ratio band structures shown in Figs. 3(a) and 3(b) for the corresponding viscous and viscoelastic phononic composite beams, respectively. Unlike the plain beams, the band structures expectedly capture Bragg bandgaps spanning two different frequency regions (10.14-13.58 kHz and 30.01-36.19 kHz). Again, the viscous and viscoelastic beams produce identical results for a large μ_b value, and similar observations can be made about Figs. 2(c) and 3(c), with the exception of Bloch damping ratio solutions that are notably absent within the bandgap region in Fig. 3(c). Another important observation is that the existence of a Bragg bandgap in a given phononic beam does not fundamentally influence its damping behavior. Finally, it is worthy noting that "band-overtaking" takes place in both Figs. 2(a) and 3(a), which is a phenomenon associated with higher frequency bands crossing lower frequency ones as a result of increased damping levels [26].

3 Metadamping Analysis

The objective of this section is to leverage the aforementioned framework to investigate viscoelastic metadamping in polymeric composite metamaterial beams, in both the infinite and finite configurations. Various phenomena exhibited in the damping-frequency band structures are herein discussed by exploring independent configurations of 1D composites comprising two viscoelastic resonators. For the basis of our comparisons, consider (1) a viscoelastic composite beam hosting two undamped resonators, (2) an undamped composite beam hosting two viscoelastic resonators. Later on, we also shed light onto the mechanics of dispersion in high damping regimes as well as the effects of different boundary conditions on the response of the damped beams.

To this end, consider a plain [0 deg] graphite-epoxy composite beam having the same geometric and material parameters given in Sec. 2.3. The lower surface of the beam is attached to a series of 12 equidistant 2-DOF (double) viscoelastic resonators that are a = 30 mm apart. Each double resonator consists of two lumped masses that are connected in series to the host beam via viscoelastic springs, as shown in Fig. 1(c). The two discrete masses are selected, such that $m_1 + m_2 = m_v$, with $m_1 = 0.35m_b$ and $m_2 = 0.05m_b$, thus ensuring an equal total mass to that of the phononic beam inspected

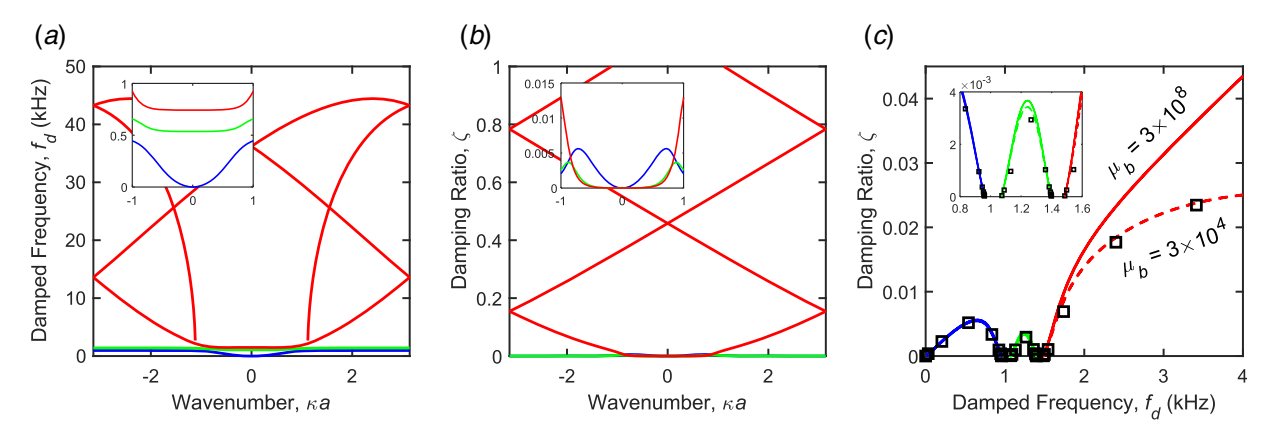


Fig. 4 (a) Frequency and (b) damping ratio band structures for a unit cell of a damped metamaterial composite beam ($\mu_b = 3 \times 10^8$) with undamped resonators ($c_1 = c_2 = 0$). (c) Damping-frequency band structure using two different relaxation parameters: (1) $\mu_b = 3 \times 10^4$ and (2) $\mu_b = 3 \times 10^8$. Modal damping ratios of the finite beam corresponding to $\mu_b = 3 \times 10^4$ are shown in (c) as discrete squares.

earlier. The first and second viscoelastic resonators are characterized by elastic stiffnesses (k_1,k_2) , viscous damping coefficients (c_1,c_2) , and relaxation parameters (μ_1,μ_2) , respectively. Moreover, the two resonators are tuned such that their natural frequencies $f_1 = (1/2\pi)\sqrt{k_1/m_1}$ and $f_2 = (1/2\pi)\sqrt{k_2/m_2}$ are equal with $f_1 = f_2 = 1160 \, \text{Hz}$.

3.1 Influence of Structural Viscoelasticity. The first configuration consists of a viscoelastic composite beam hosting two undamped resonators ($c_1 = c_2 = 0$). Consistent with the plain and phononic beams in Sec. 2.3, the same proportionality constant $(\alpha = 3.58 \times 10^{-6})$ is used for the hosting beam. Figures 4(a) and 4(b) depict the frequency and damping ratio band structures for a representative unit cell with $\mu_b = 3 \times 10^8$. More importantly, these two figures are complemented with close-up insets, revealing band hybridizations that are associated with local resonance bandgaps spanning two different frequency zones (959.8-1072 Hz and 1398–1484 Hz), which lie below and above the resonator's tuning frequency. Figure 4(c), on the other hand, displays the dampingfrequency band structure using two relaxation parameters: μ_b = 3×10^4 and $\mu_b = 3 \times 10^8$, complemented with the modal damping ratios of the finite beam corresponding to the first μ_b value. The close-up inset provided in Fig. 4(c) reveals that this particular configuration is responsible for producing substantially small damping ratios around the edges of both bandgaps, irrespective of the viscoelasticity level in the beam. Such unique behavior was absent from the phononic beam (see Fig. 3(c)) and is attributed to the local resonance properties of the metamaterial beam. Another critical aspect throughout this effort is how Bloch damping ratios corresponding to the second band (henceforth plotted in green to distinguish it from other bands) change as a function of frequency. To fully understand this, an in-depth study of the viscoelastic effects emerging from the local resonators is required as will be outlined next. Finally, it is worthwhile to mention that for the current configuration, the second band follows a concave-down path.

3.2 Influence of Resonator Viscoelasticity. Second, we consider a configuration where an undamped composite beam ($\alpha = 0$) hosts two viscoelastic resonators. Such configuration can further be subdivided into (1) a metamaterial with a viscoelastic first resonator and an undamped second resonator and (2) a metamaterial where the first resonator is undamped, while the second is viscoelastic. The motivation behind this classification will become apparent shortly. Starting with the first metamaterial, Figs. 5(a) and 5(b)show the frequency and damping ratio band structures when the first resonator is viscoelastic with $\zeta_1 = 0.003$ and $\mu_1 = 10^6$, while the second resonator is undamped $(c_2 = 0)$. The local resonance bandgaps induced in this case are found to be identical to the ones corresponding to the first configuration in Sec. 3.1. Figure 5(c) depicts the damping behavior of the metamaterial in the 0-4 kHz frequency range. It shows that damping in the first resonator is mainly responsible for amplifying the Bloch damping ratios

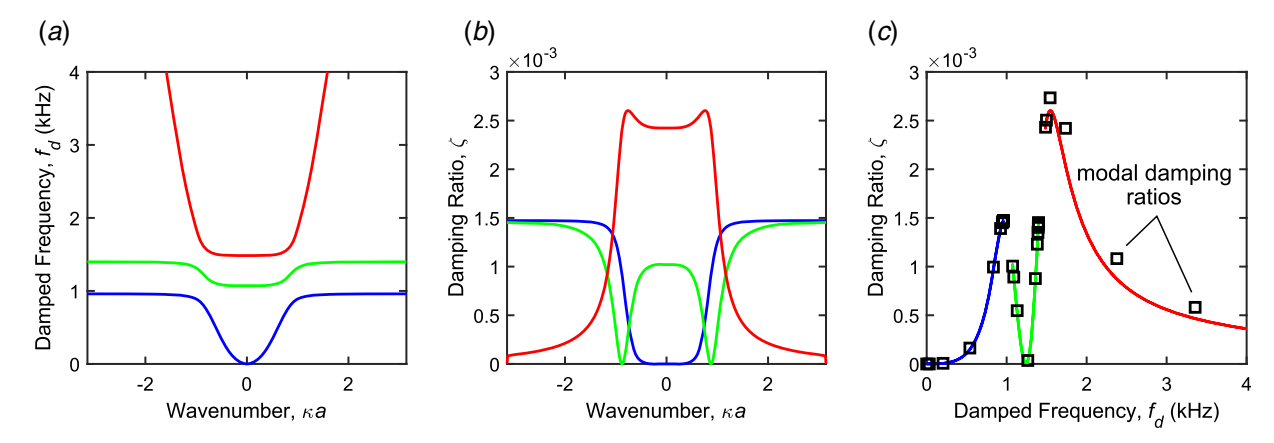


Fig. 5 (a) Frequency, (b) damping ratio, and (c) damping-frequency band structures for a unit cell of an undamped metamaterial composite beam ($\alpha = 0$) with viscoelastic first resonator ($\mu_1 = 10^6$) and undamped second resonator ($\mu_2 = 0$). Modal damping ratios of the finite beam are shown in (c) as discrete squares.

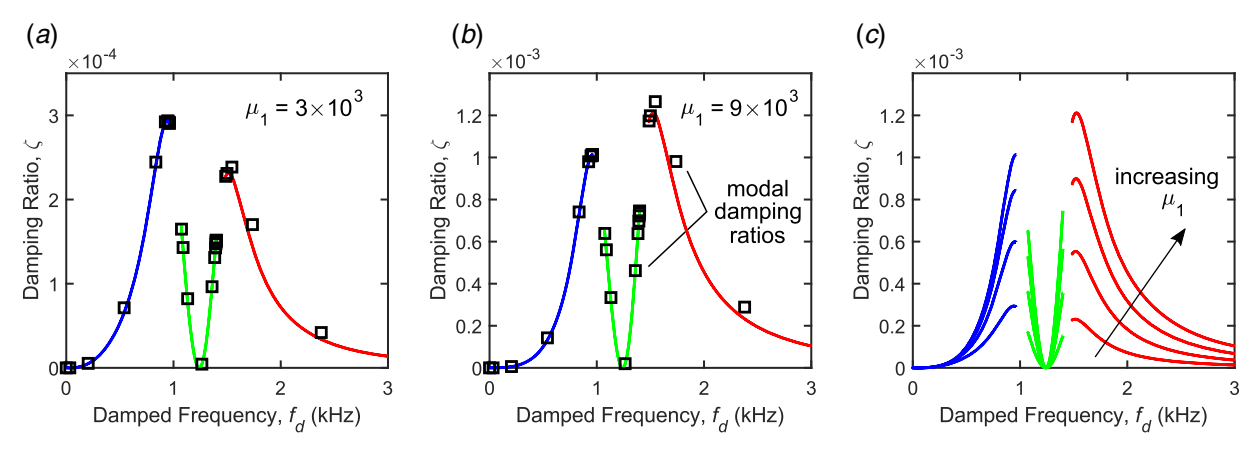


Fig. 6 Damping-frequency band structures for a unit cell of an undamped metamaterial composite beam (α = 0) with viscoelastic first resonator and undamped second resonator (c_2 = 0). The relaxation parameter of the first resonator is selected as follows: (a) μ_1 = 3 × 10³ and (b) μ_1 = 9 × 10³. (c) The evolution of the beam's damping behavior using several relaxation parameters.

around both bandgap edges. More interestingly, the second band separating the two bandgaps now exhibits a concave-up shape. The previous damping features are validated by plotting modal damping ratios of the finite beam in the same figure. Furthermore, unique viscoelastic characteristics of the metamaterial under consideration can be interpreted graphically by computing dampingfrequency band structures using different relaxation parameters. For example, Figs. 6(a) and 6(b) correspond to $\mu_1 = 3 \times 10^3$ and $\mu_1 = 9 \times 10^3$, respectively. A careful inspection of both figures reveals a change in the damping behavior. For $\mu_1 = 3 \times 10^3$, the maximum attainable Bloch and modal damping ratios of the acoustic band (blue) are larger than their optical band counterparts (red). As such, the second band starts with higher damping ratios than those which appear at the band end. As the relaxation parameter increases to $\mu_1 = 9 \times 10^3$, this behavior is reversed and the maximum attainable Bloch and modal damping ratios of the acoustic band become smaller than their optical band counterparts, with the second band starting with lower damping ratios than those at its end. In Fig. 6(c), the damping-frequency band structure is computed using several relaxation parameters. It shows that at a certain threshold of the viscoelasticity level in the first resonator, the damping behavior of the resultant metamaterial switches as discussed earlier. Nonetheless, the second band maintains the concave-up shape for all the relaxation parameters used to construct

The mechanism of energy dissipation due to the second resonator is radically different. Figures 7(a) and 7(b) show the frequency and

damping ratio band structures, respectively, for a metamaterial beam with an undamped first resonator $(c_1 = 0)$ and a viscoelastic second resonator with $\zeta_2 = 0.003$ and $\mu_2 = 10^6$. While some features corresponding to the previous metamaterial (with $\mu_1 = 10^6$ and $c_2 =$ 0) remain unchanged, such as for example the frequency regions spanned by both bandgaps (depicted in Fig. 7(a)) and the general shape of the acoustic and optical bands in Fig. 7(c), a unique and distinguishable feature of the current metamaterial can be clearly seen from the shape of the second band in Fig. 7(c), which reveals a concave-down formation in contrast to Fig. 5(c). To explore the evolution of the metamaterial's behavior as a function of μ_2 , damping-frequency band structures are computed in Figs. 8(a) and 8(b) using $\mu_2 = 10^3$ and $\mu_2 = 5 \times 10^4$, respectively. Similar observations to the ones made in Figs. 6(a) and 6(b) can be made here as well. In brief, the principal difference between Figs. 8(a) and 8(b) is a dissipative interchanging behavior. Finally, Fig. 8(c) reveals that as μ_2 increases gradually, the resultant metamaterial switches its damping behavior at some point. However, once again, the second bands exhibit a concave-down shape for all the selected values of μ_2 .

Designing such structures with multiple bandgaps can be serviceable in many applications that require vibroacoustic attenuation across broadband frequency ranges or even narrow yet distinct ones. However, a major hurdle is the existence of a number of unavoidable vibration modes between every two consecutive bandgaps. Consequently, a natural question that arises from this discussion is whether it is possible to mitigate such vibration modes without

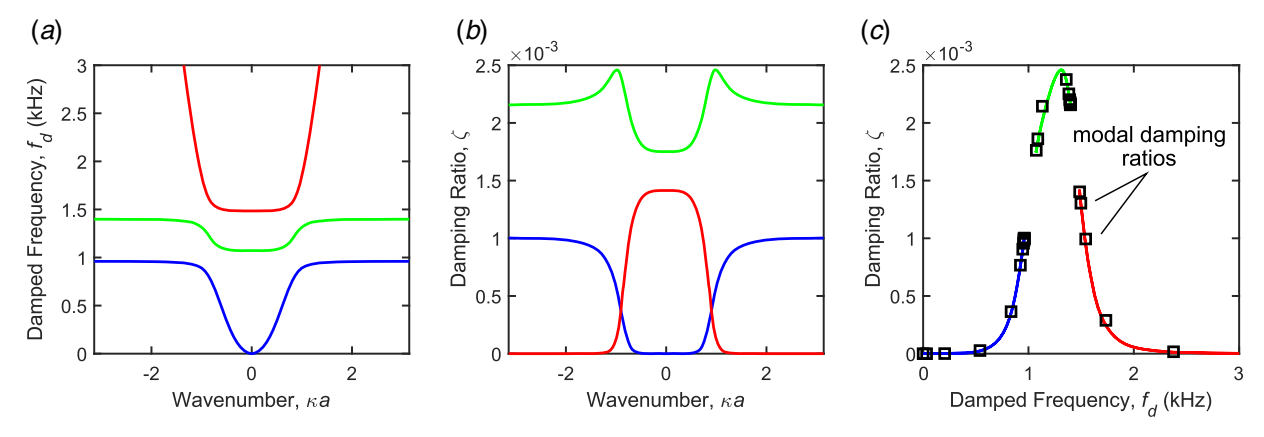


Fig. 7 (a) Frequency, (b) damping ratio, and (c) damping-frequency band structures for a unit cell of an undamped metamaterial composite beam ($\alpha = 0$) with undamped first resonator ($c_1 = 0$) and viscoelastic second resonator ($\mu_2 = 10^6$). Modal damping ratios of the finite beam are shown in (c) as discrete squares.

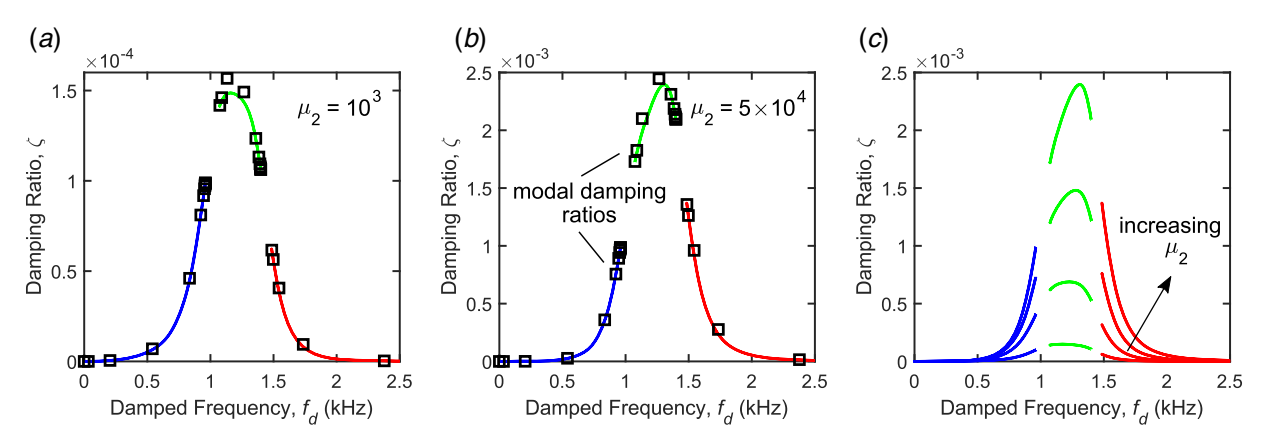


Fig. 8 Damping-frequency band structures for a unit cell of an undamped metamaterial composite beam $(\alpha = 0)$ with undamped first resonator $(c_1 = 0)$ and viscoelastic second resonator. The relaxation parameter of the second resonator is selected as follows: (a) $\mu_2 = 10^3$ and (b) $\mu_2 = 5 \times 10^4$. (c) The evolution of the beam's damping behavior using several relaxation parameters.

compromising on the efficiency of the induced bandgaps. Previous efforts have already shown that excessive amounts of damping can very well cause bandgap curtailment in locally resonant metamaterials [23]. In particular, incorporating damping in the local resonators without sufficient knowledge can cause severe damage to the metamaterial's dynamic performance. As such, it is imperative to be conscious of dissipative losses in the local resonators when designing multibandgap metamaterials. To this end, we assemble Figs. 9(a)-9(c), which display the band structures in Fig. 7 superimposed on their corresponding counterparts in Fig. 5. They represent a fair comparison between the metamaterial's behavior when dissipative effects arise due to the first resonator (alone) or the second resonator (alone), ensuring equal damping amounts in both resonators.

Two main observations can be drawn from Fig. 9(c): (1) while both resonators affect the acoustic and optical bands in the same fashion, amplifying their associated Bloch damping ratios around the bandgap edges, the first resonator is more efficient than the second resonator in attaining such amplification. Moreover, it is clear that damping in the first resonator impacts a wider range of frequencies than the second resonator does. (2) Damping in the second resonator is more authoritative than damping in the first resonator for achieving vibration attenuation between induced bandgaps. The validity of these observations, obtained from unit cell dispersion analyses, can be readily checked by plotting frequency response functions (FRFs) of the corresponding finite beams as shown in Fig. 9(d). Forces with magnitudes of 1 N are applied at 30 mm

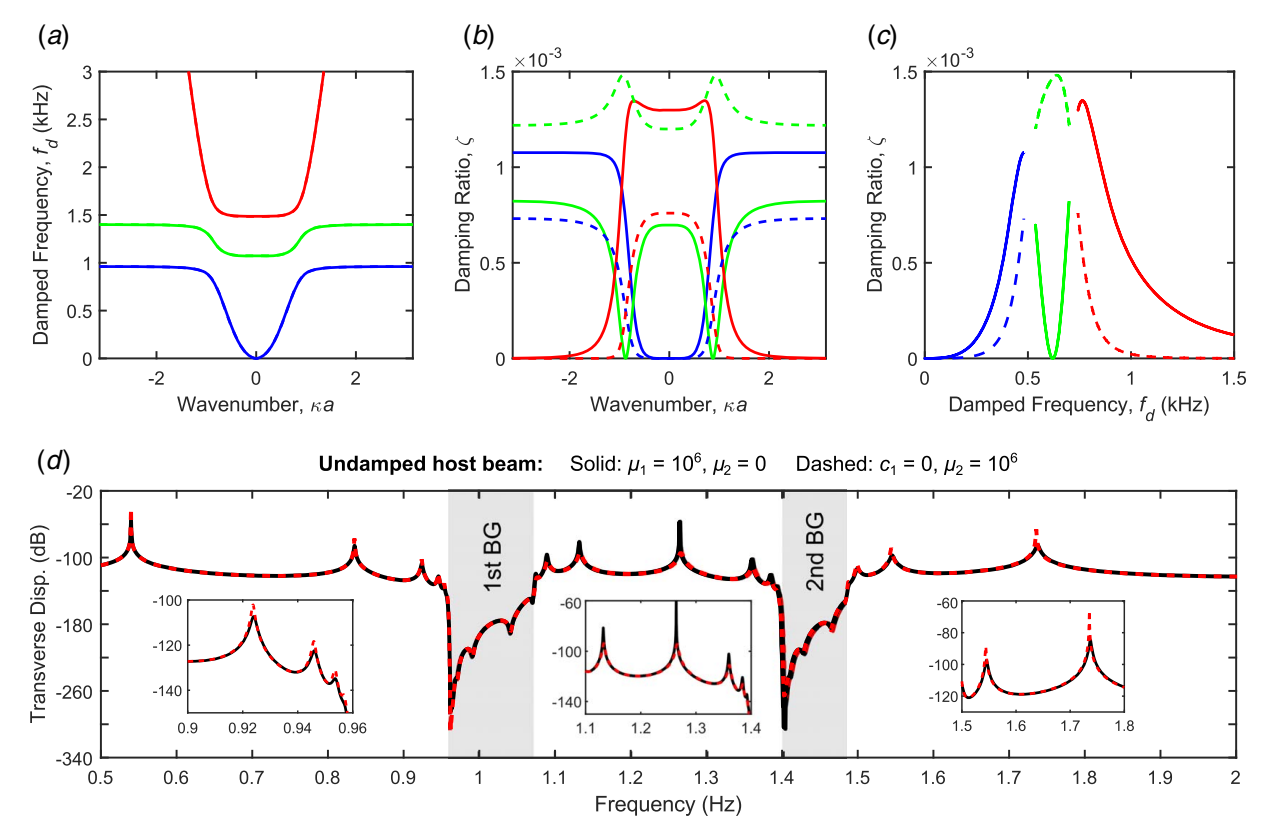


Fig. 9 A comparison between the (a) frequency, (b) damping ratio, and (c) damping-frequency band structures for the unit cell studied in Fig. 5 (solid) and the unit cell studied in Fig. 7 (dotted). (d) A comparison between FRFs of two finite metamaterial beams corresponding to the unit cells used in (a)–(c).

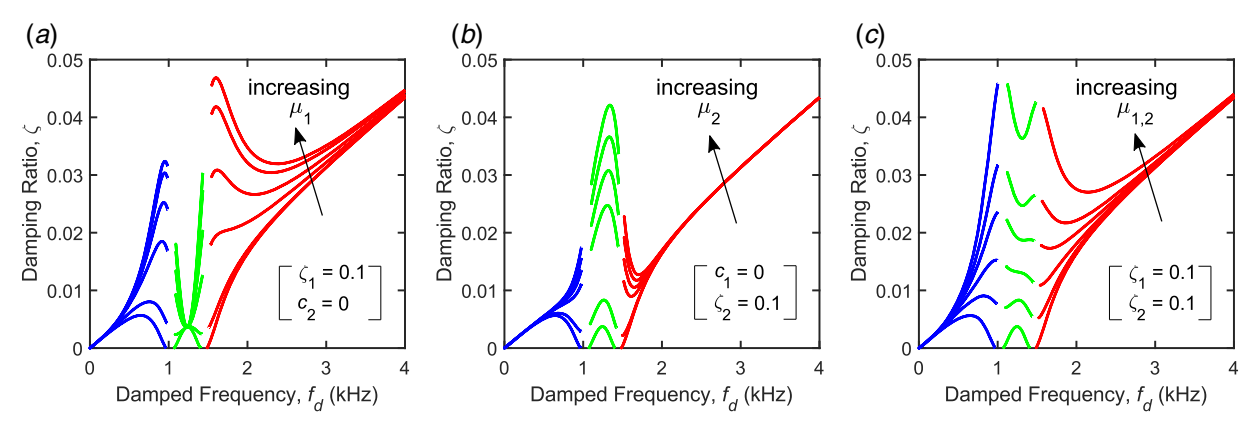


Fig. 10 Damping-frequency band structures for a unit cell of a damped metamaterial composite beam ($\mu_b = 10^6$) with (a) viscoelastic first resonator and undamped second resonator ($c_2 = 0$), (b) undamped first resonator ($c_1 = 0$) and viscoelastic second resonator, and (c) viscoelastic first and second resonators. Each figure is computed using several relaxation parameters, revealing unique damping characteristics associated with each resonator damping arrangement.

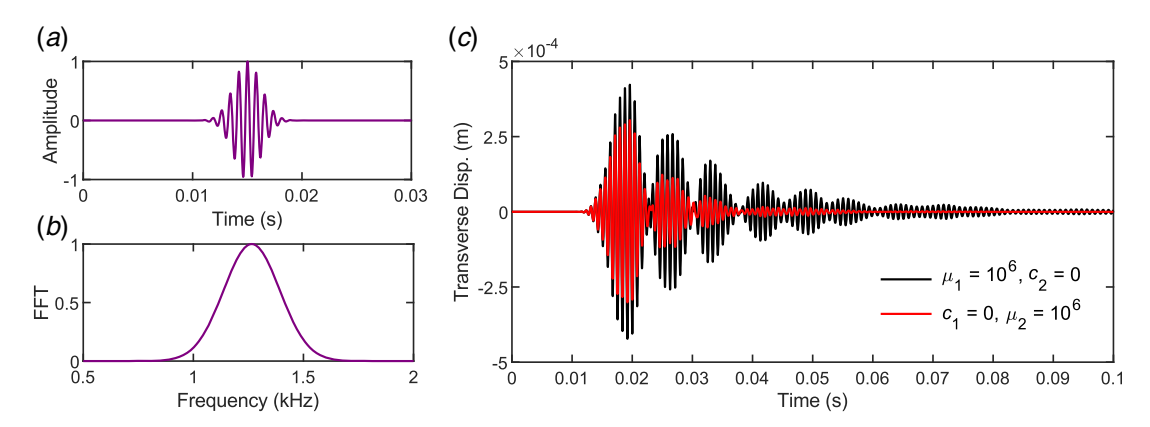


Fig. 11 (a) A normalized Gaussian pulse and (b) its corresponding Fourier spectrum. (c) A comparison between the temporal responses of two damped metamaterial composite beams ($\mu_b = 10^6$) with (1) viscoelastic first resonator and undamped second resonator (black) and (2) undamped first resonator and viscoelastic second resonator (red), under the application of the transient excitation given in (a).

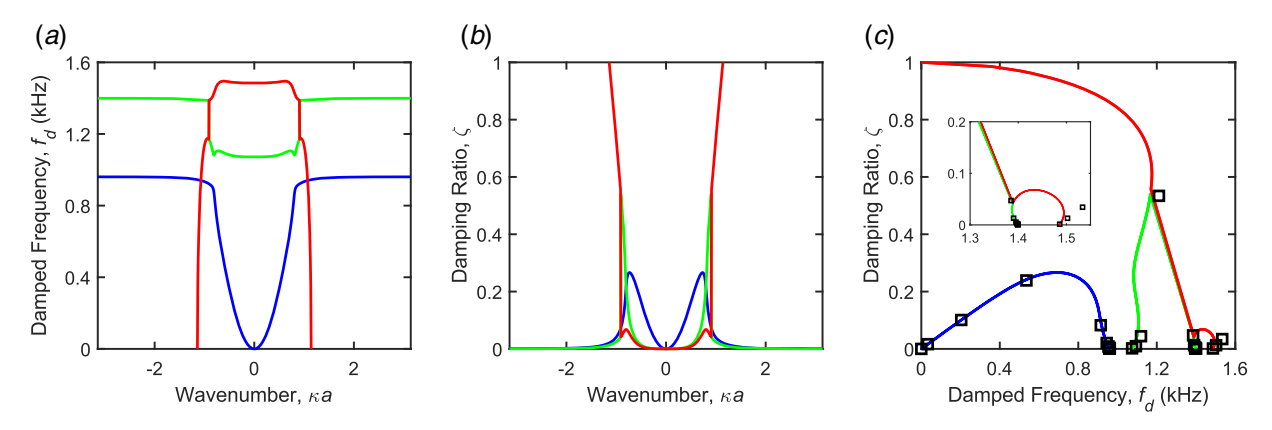


Fig. 12 (a) Frequency, (b) Damping ratio, and (c) Damping-frequency band structures for a unit cell of a highly damped metamaterial composite beam $(\mu_b = 3 \times 10^8)$ with undamped resonators $(c_1 = c_2 = 0)$. Modal damping ratios of the finite beam are shown in (c) as discrete squares.

from the fixed ends of both beams, and the corresponding transverse displacements are calculated at the beam tips. The three close-up insets provided in Fig. 9(d) clearly confirm the main observations stated earlier. However, the effects of resonator damping will be revisited when the time domain analysis is conducted in Sec. 3.3.

3.3 Influence of Combined Viscoelasticity. A more realistic configuration is one which accounts for simultaneous viscoelastic dissipation from the composite beam and the local resonators. For brevity, only damping-frequency band structures will be used to study this configuration as shown in Fig. 10. All displayed subfigures

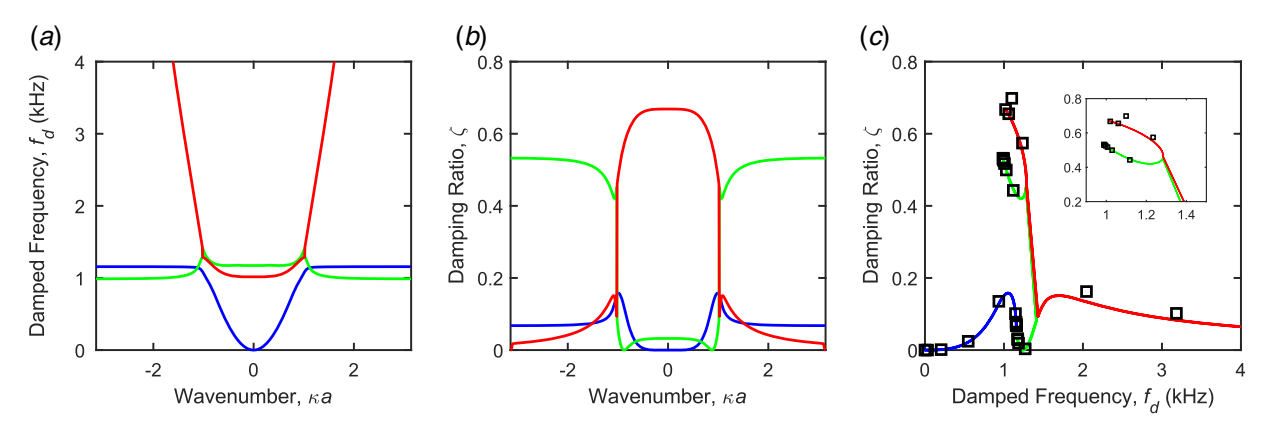


Fig. 13 (a) Frequency, (b) damping ratio, and (c) damping-frequency band structures for a unit cell of an undamped metamaterial composite beam ($\alpha = 0$) with highly damped viscoelastic first resonator ($\mu_1 = 10^6$) and undamped second resonator ($\epsilon_2 = 0$). Modal damping ratios of the finite beam are shown in (c) as discrete squares.

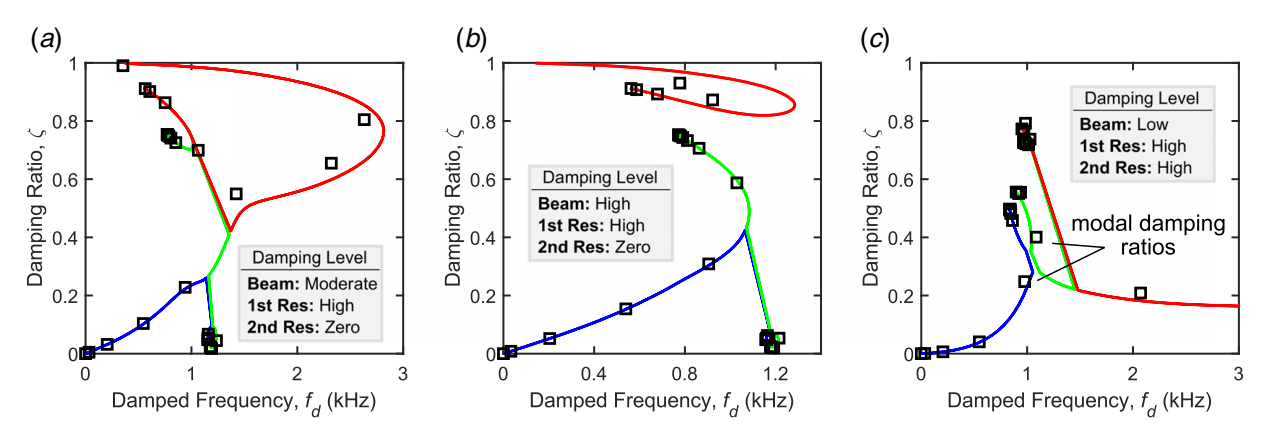


Fig. 14 Damping-frequency band structures for a unit cell of (a) a moderately damped composite beam with highly damped first resonator, (b) a highly damped composite beam with highly damped first resonator, and (c) a lightly damped composite beam with highly damped first and second resonators. Modal damping ratios of the corresponding finite beams are shown as discrete squares.

are obtained for a viscoelastic composite beam with $\mu_b = 10^{\circ}$. However, each subfigure is associated with a unique resonator damping arrangement. For the first subfigure (Fig. 10(a)), the first resonator is viscoelastic ($\zeta_1 = 0.1$), while the second is kept undamped $(c_2 = 0)$. A number of band structures are computed for relaxation parameters ranging between $\mu_1 = 2 \times 10^2$ and $\mu_1 = 10^4$. The results reveal that not all the corresponding second bands have the same shape. For relatively small relaxation parameters (e.g., $\mu_1 = 2 \times 10^2$), resulting second bands exhibit concave-down formations. However, as μ_1 gradually increases, the shape of the second band changes in return, switching to a concave-up formation at some transition point and maintaining the new shape beyond that point. Changing the damping behavior in this manner implies that the second band shape is controlled by the relative damping of the structure and viscoelastic resonators. In Fig. 10(b), the first resonator is undamped $(c_1 = 0)$, whereas the second is viscoelastic $(\zeta_2 = 0.1)$ with relaxation parameters ranging between $\mu_2 = 2 \times 10^2$ and $\mu_2 = 8 \times 10^3$. Unlike the previous resonator damping arrangement, this one is associated with concave-down second bands for all the considered μ_2 values, which confirms the authority of the second resonator on the second band's damping behavior, irrespective of the viscoelasticity level in the hosting beam. Finally, when both resonators are viscoelastic with $\zeta_1 = \zeta_2 = 0.1$, Fig. 10(c) displays the corresponding band structure for relaxation parameters ranging between $\mu_1 = \mu_2 = 2 \times 10^2$ and $\mu_1 = \mu_2 = 7 \times 10^3$. In this case, the combined mechanism of dissipation from all possible

damping sources yields the second band formations shown in the figure.

In summary, although the mechanics of dispersion in multibandgap metamaterials are fundamentally controlled by the relative damping of the hosting structure and the resonant inclusions, each resonator damping arrangement is shown to be associated with its own damping characteristics as discussed earlier. For a given finite metamaterial beam, it is interesting to see how different arrangements impact the temporal response in the context of a timetransient analysis. To execute this task, let us consider two finite cantilevered metamaterials that are both assembled from the same viscoelastic beam ($\alpha = 1.19 \times 10^{-5}$ and $\mu_b = 10^6$). However, it is assumed that the first beam is integrated with a viscoelastic first resonator ($\zeta_1 = 0.015$ and $\mu_1 = 10^6$) and an undamped second resonator $(c_2 = 0)$, whereas the second beam is integrated with an undamped first resonator ($c_1 = 0$) and a viscoelastic second resonator $(\zeta_2 = 0.015 \text{ and } \mu_2 = 10^6)$. Figure 11(c) shows a comparison between the temporal responses of the two beams when equal forces are applied at 30 mm from their fixed ends. Displacements are calculated at the beam tips when excitations of the form f(t) = $F_0 e^{-(t-t_0)^2/2\sigma^2} \cos(2\pi f_c t)$ are applied such that the different parameters in the equation are given as follows: $F_o = 500 \,\mathrm{N}$, $t_o = 15 \,\mathrm{ms}$, $\sigma =$ 1.25 ms, and $f_c = 1265$ Hz. The parameters are carefully selected to represent a Gaussian pulse (Fig. 11(a)), which mainly impacts the second band with a spectral content that is centered around f_c as depicted from the corresponding Fourier spectrum in Fig. 11(b).

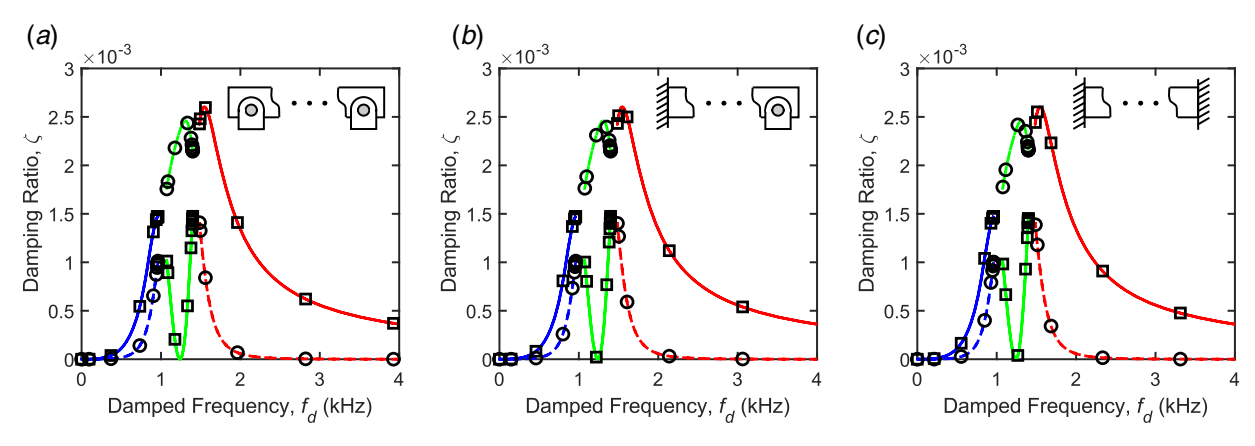


Fig. 15 Modal damping ratios of finite beams with three different physical boundary conditions: (a) hinged-hinged, (b) fixed-hinged, and (c) fixed-fixed, superimposed on the damping-frequency band structures computed from their representative unit cells

The comparison shown in Fig. 11(c) validates the findings of Sec. 3.2.

3.4 Influence of High Viscoelastic Damping. As discussed earlier, refraining from using excessive damping in locally resonant metamaterials is often essential to avoid performance deterioration. However, such undesirable performance is yet to be investigated in the context of unit cell predictions. To better understand the mechanics of dispersion within high damping regimes, different energy dissipation sources will be analyzed individually then in combined form. First, only structural damping is increased (α = 1.59×10^{-4} and $\mu_b = 3 \times 10^8$), while both resonators are kept undamped. Figure 12(a) shows that the second bandgap disappears completely although operating in the oscillatory frequency range. The first bandgap is not terminated but is curtailed to a certain extent (it would completely disappear if structural damping is further increased—not shown here for brevity). Moreover, Bloch damping ratios in the third band are shown to increase until reaching the nonoscillatory zone (Fig. 12(b)). Bandgap termination in this particular case (with high structural damping) manifests itself in the damping-frequency band structure in intriguing fashion that can be clearly noticed from the close-up inset in Fig. 12(c). It can be seen that upon reaching a certain point, the second and third bands drop abruptly, heading down in the same direction before splitting in opposite directions at some lower damping point. Such behavior can be realized by superimposing modal damping ratios of the corresponding finite beam on the same figure. The obtained results reveal that as long as the resonators are undamped, the metamaterial beam will still produce frequency regions associated with strong oscillations, regardless of the existence/absence of a frequency bandgap and irrespective of the damping level in the hosting beam. Conversely, when the damping level in the resonators is increased while the host beam is kept undamped, the resulting dispersion characteristics substantially change. Consider a case where only the first resonator is highly damped ($\zeta_1 = 0.6$ and $\mu_1 =$ 10^{6}), while the second resonator is undamped. Figures 13(a) and 13(b) show that all three bands intersect with each other, terminating both bandgaps even before reaching the nonoscillatory zone. A notable feature of Fig. 13(c) is the mechanism of the second bandgap termination, which shows that on reaching a certain point, the second and third bands rise abruptly, heading up in the same direction before splitting in opposite directions at some higher damping point. This behavior can be realized by superimposing modal damping ratios of the corresponding finite beam on the same figure. Finally, the combined effect of high structural and resonator damping is shown in Fig. 14 for three different cases: (1) moderate structural damping combined with high first resonator damping as shown in Fig. 14(a), (2) high structural damping

combined with high first resonator damping as shown in Fig. 14(b), and (3) light structural damping combined with high damping in both resonators as shown in Fig. 14(c). All three cases demonstrate the complete extinction of frequency bandgaps as a result of cumulative damping. Dispersion characteristics similar to the ones deduced from Figs. 12 and 13 are also observed in Fig. 14. It should be noted that these cases represent only a few examples of an infinite number of possible damping combinations. Nevertheless, we believe the results presented here describe the most important dispersion features encountered in locally resonant metamaterials.

3.5 Influence of Physical Boundary Conditions. All the infinite medium predictions have thus far been validated using finite beams with only one type of physical boundary conditions, namely, fixed-free (or cantilever). We briefly demonstrate the robustness of such unit cell predictions by considering finite beams with three different physical boundary conditions: (1) hinged-hinged, (2) fixed-hinged, and (3) fixed-fixed. In Fig. 15, the modal damping ratios of each finite beam are computed and superimposed on the damping-frequency band structure obtained from a representative unit cell to produce three subfigures similar to the one provided in Fig. 9(c). Interestingly, vibration modes close to bandgap regions exhibit damping ratios that are only very minimally affected by the type of boundary conditions. These results confirm that the most important metadamping features are predominantly controlled by the presence of the resonant inclusions in multibandgap metamaterials.

4 Design for Multiple Bandgaps

To provide general guidelines for the design of multibandgap viscoelastic metamaterials, consider an undamped composite beam (α =0) leveraging triple serially connected local resonators. To understand the sole damping effect from each resonator, Fig. 16 is created. Each of its three subfigures depict the metadamping mechanics when two resonators are kept undamped, while the third is rendered lossy with ζ =0.003 and μ =3×108:

- When only the first resonator is damped and the second and third are kept undamped $(c_2 = c_3 = 0)$, resulting intermediate bands (second and third) produce the concave-up formations shown in Fig. 16(a). The previous implies that this particular resonator damping arrangement produces substantially small Bloch damping ratios at some intermediate points through each of these two intermediate bands.
- When only the second resonator is damped while the first and third are kept undamped $(c_1 = c_3 = 0)$, the second band ends with substantially small Bloch damping ratios, while the

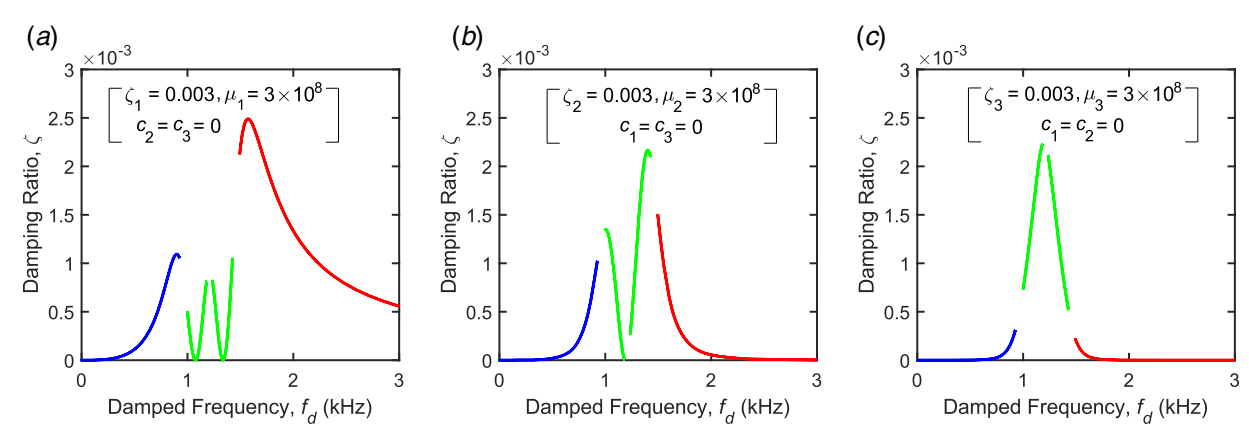


Fig. 16 Damping-frequency band structures for a unit cell of an undamped metamaterial composite beam ($\alpha = 0$) with viscoelastic damping in the (a) first resonator alone, (b) second resonator alone, and (c) third resonator alone

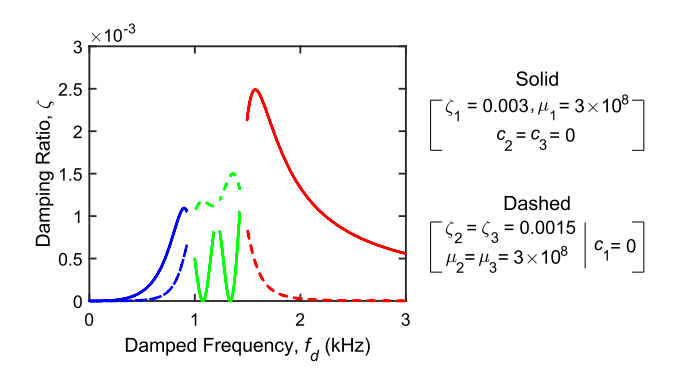


Fig. 17 A comparison between the damping-frequency band structures for a unit cell of an undamped metamaterial composite beam (α = 0) with (1) viscoelastic damping in the first resonator alone (solid) and (2) combined viscoelastic damping in the second and third resonators (dotted)

third band begins with relatively small Bloch damping ratios ($\zeta < 0.5 \times 10^{-3}$) as shown in Fig. 16(*b*). Moreover, this resonator damping arrangement is less efficient than the previous one in terms of attenuating vibration modes belonging to the acoustic (blue, leftmost) and optical (red, rightmost) bands.

• When only the third resonator is damped while the first and second are kept undamped $(c_1 = c_2 = 0)$, relatively small Bloch damping ratios are observed at the start of the second band $(\zeta \cong 0.7 \times 10^{-3})$ as well as at the end of the third band $(\zeta \cong 0.5 \times 10^{-3})$ as shown in Fig. 16(c). Furthermore, this resonator damping arrangement is the least efficient in attenuating vibration modes belonging to the acoustic (blue, leftmost) and optical (red, rightmost) bands.

To achieve broadband vibroacoustic attenuation that extends from the beginning of (and slightly before) the first bandgap to the end of (and slightly after) the third bandgap, it is clear that between the three arrangements discussed earlier, the third is the best choice. However, such damping performance can be further enhanced by utilizing an arrangement that incorporates simultaneous and concurrent damping in both the second and third resonators. To ensure a fair comparison, total damping ($\zeta = 0.003$) is equally divided between the second and third resonators such that $\zeta_2 = \zeta_3 = 0.0015$ with $\mu_2 = \mu_3 = 3 \times 10^8$ to produce the damping-frequency band structure shown in Fig. 17, which is superimposed on its counterpart from Fig. 16(a). Upon careful inspection of this figure, it is clear that the second and third bands produce concavedown formations that exhibit Bloch damping ratios >0.001 without compromising on the efficiency of the induced bandgaps.

5 Conclusions

An in-depth analysis of the elastic wave dispersion mechanics was conducted in this article to investigate the viscoelastic damping behavior of infinite as well as finite 1D polymeric composite metamaterials with multiple bandgaps. The applied free wave unit cell model was derived based on well-established theories in linear viscoelasticity and wave propagation in periodic solids. The proposed framework was validated against commonly used benchmark viscous damping models. Following this, the model was deployed to elucidate the viscoelastic metadamping phenomenon in a graphite-epoxy metamaterial beam comprising periodic double and triple resonators. It was concluded that the dispersion mechanics associated with a given metamaterial are highly sensitive to the chosen resonator damping arrangement. Specifically, for a double resonator metamaterial beam, it has been found that while both resonators affect the acoustic and optical bands in the same fashion, amplifying their associated Bloch damping ratios around the bandgap edges, the first resonator is more efficient than the second resonator in attaining such amplification. Moreover, damping in the first resonator was shown to be capable of affecting a wider range of frequencies than the second resonator. Conversely, damping in the second resonator is more authoritative than damping in the first resonator for achieving vibration attenuation between induced bandgaps. Depending on the selected resonator damping arrangement, damping-frequency band structures generate intermediate bands with different shapes and concavities, the understanding of which is critical to the effective design of bandgap structures for applications that require vibroacoustic attenuation across broadband frequency ranges (or even narrow yet distinct ones). Finally, the robustness of the unit cell predictions has been demonstrated. Results show that vibration modes close to bandgap regions exhibit damping ratios that are only minimally affected by the type of boundary conditions, implying that the most important metadamping features are predominantly controlled by the presence of the resonant inclusions in multibandgap metamaterials.

Acknowledgment

M. Nouh acknowledges the support of this work from the US National Science Foundation through Award no. 1847254 (CAREER).

Conflicts of Interest

There are no conflicts of interest.

Data Availability Statement

The datasets generated and supporting the findings of this article are obtainable from the authors upon reasonable request. The authors attest that all data for this study are included in the paper.

References

- Park, J., Lee, D., and Rho, J., 2020, "Recent Advances in Non-Traditional Elastic Wave Manipulation by Macroscopic Artificial Structures," Appl. Sci., 10(2), p. 547.
- [2] Al Ba'ba'a, H., Attarzadeh, M., and Nouh, M., 2018, "Experimental Evaluation of Structural Intensity in 2d Plate-type Locally Resonant Elastic Metamaterials," ASME J. Appl. Mech., 85(4), p. 041005.
- [3] Liu, L., and Hussein, M. I., 2012, "Wave Motion in Periodic Flexural Beams and Characterization of the Transition Between Bragg Scattering and Local Resonance," ASME J. Appl. Mech., 79(1), p. 011003.
- [4] Hu, G., Tang, L., Xu, J., Lan, C., and Das, R., 2019, "Metamaterial With Local Resonators Coupled by Negative Stiffness Springs for Enhanced Vibration Suppression," ASME J. Appl. Mech., 86(8), p. 081009.
- [5] Chen, J.-S., and Chien, I., 2017, "Dynamic Behavior of a Metamaterial Beam With Embedded Membrane-Mass Structures," ASME J. Appl. Mech., 84(12), p. 121007.
- [6] Al Ba'ba'a, H., Nouh, M., and Singh, T., 2017, "Formation of Local Resonance Band Gaps in Finite Acoustic Metamaterials: A Closed-Form Transfer Function Model," Sound Vib J, 410, pp. 429–446.
- [7] Baz, A., 2019, "Active Acoustic Metamaterial With Tunable Effective Density Using a Disturbance Rejection Controller," J. Appl. Phys., 125(7), p. 074503.
- [8] He, Z.-H., Wang, Y.-Z., and Wang, Y.-S., 2019, "Active Feedback Control on Sound Radiation of Elastic Wave Metamaterials," AIAA J., 57(10), pp. 4536–4547.
- [9] Rong, J., and Ye, W., 2019, "Topology Optimization Design Scheme for Broadband Non-Resonant Hyperbolic Elastic Metamaterials," Comput. Methods Appl. Mech. Eng., 344, pp. 819–836.
- [10] Vila, J., Paulino, G. H., and Ruzzene, M., 2019, "Role of Nonlinearities in Topological Protection: Testing Magnetically Coupled Fidget Spinners," Phys. Rev. B, 99(12), p. 125116.
- [11] Aladwani, A., Almandeel, A., and Nouh, M., 2019, "Fluid-Structural Coupling in Metamaterial Plates for Vibration and Noise Mitigation in Acoustic Cavities," Int. J. Mech. Sci., 152, pp. 151–166.
- [12] Attarzadeh, M., Al Ba'ba'a, H., and Nouh, M., 2018, "On the Wave Dispersion and Non-Reciprocal Power Flow in Space-Time Traveling Acoustic Metamaterials," Appl. Acoustics, 133, pp. 210–214.
- [13] Serra-Garcia, M., Peri, V., Süsstrunk, R., Bilal, O. R., Larsen, T., Villanueva, L. G., and Huber, S. D., 2018, "Observation of a Phononic Quadrupole Topological Insulator," Nature, 555(7696), pp. 342–345.
- [14] Verdier, M., Lacroix, D., and Termentzidis, K., 2017, "Heat Transport in Phononic-Like Membranes: Modeling and Comparison With Modulated Nano-Wires," Int. J. Heat. Mass. Transfer., 114, pp. 550–558.
- [15] Sena-Junior, M. I., Lima, L. R., and Lewenkopf, C. H., 2017, "Phononic Heat Transport in Nanomechanical Structures: Steady-State and Pumping," J. Phys. A: Math. Theor., 50(43), p. 435202.
- [16] Attarzadeh, M., Callanan, J., and Nouh, M., 2020, "Experimental Observation of Nonreciprocal Waves in a Resonant Metamaterial Beam," Phys. Rev. Appl., 13(2), p. 021001.
- [17] Moore, K. J., Bunyan, J., Tawfick, S., Gendelman, O. V., Li, S., Leamy, M., and Vakakis, A. F., 2018, "Nonreciprocity in the Dynamics of Coupled Oscillators With Nonlinearity, Asymmetry, and Scale Hierarchy," Phys. Rev. E, 97(1), p. 012219.
- [18] Al Ba'ba'a, H., and Nouh, M., 2017, "An Investigation of Vibrational Power Flow in One-Dimensional Dissipative Phononic Structures," ASME J. Vib. Acoust., 139(2), p. 021003.
- [19] Al Ba'ba'a, H. B., and Nouh, M., 2017, "Mechanics of Longitudinal and Flexural Locally Resonant Elastic Metamaterials Using a Structural Power Flow Approach," Int. J. Mech. Sci., 122, pp. 341–354.
- [20] Hussein, M. I., and Frazier, M. J., 2013, "Metadamping: An Emergent Phenomenon in Dissipative Metamaterials," J. Sound. Vib., 332(20), pp. 4767– 4774.
- [21] Frazier, M. J., and Hussein, M. I., 2015, "Viscous-to-Viscoelastic Transition in Phononic Crystal and Metamaterial Band Structures," J. Acoust. Soc. Am., 138(5), pp. 3169–3180.
- [22] DePauw, D., Al Ba'ba'a, H., and Nouh, M., 2018, "Metadamping and Energy Dissipation Enhancement Via Hybrid Phononic Resonators," Extreme Mech. Lett., 18, pp. 36–44.

- [23] Aladwani, A., and Nouh, M., 2020, "Mechanics of Metadamping in Flexural Dissipative Metamaterials: Analysis and Design in Frequency and Time Domains," Int. J. Mech. Sci., 173, p. 105459.
- [24] Cajić, M., Karličić, D., Paunović, S., and Adhikari, S., 2020, "A Fractional Calculus Approach to Metadamping in Phononic Crystals and Acoustic Metamaterials," Theoretical and Applied Mechanics, 47, p. 3.
- [25] Bacquet, C. L., and Hussein, M. I., 2018, "Dissipation Engineering in Metamaterials by Localized Structural Dynamics," arXiv preprint.
- [26] Bacquet, C. L., Al Ba'ba'a, H., Frazier, M. J., Nouh, M., and Hussein, M. I., 2018, "Chapter Two-Metadamping: Dissipation Emergence in Elastic Metamaterials," Adv. Appl. Mech., 51, pp. 115–164.
- [27] Treviso, A., Van Genechten, B., Mundo, D., and Tournour, M., 2015, "Damping in Composite Materials: Properties and Models," Compos. Part B: Eng., 78, pp. 144–152.
- [28] Zhou, X., Yu, D., Shao, X., Zhang, S., and Wang, S., 2016, "Research and Applications of Viscoelastic Vibration Damping Materials: A Review," Composite Struct., 136, pp. 460–480.
- [29] Chandra, R., Singh, S., and Gupta, K., 1999, "Damping Studies in Fiber-Reinforced Composites—A Review," Composite struct., 46(1), pp. 41–51.
- [30] Chandra, R., Singh, S., and Gupta, K., 2003, "A Study of Damping in Fiber-Reinforced Composites," J. Sound. Vib., 262(3), pp. 475–496.
- [31] Zhou, X., Yu, D., Shao, X., Zhang, S., and Wang, S., 2016, "Asymptotic Analysis on Flexural Dynamic Characteristics for a Laminated Composite Plate With Embedded and Perforated Periodically Viscoelastic Damping Material Core," Composite Struct., 154, pp. 616–633.
- [32] Biswal, D. K., and Mohanty, S. C., 2019, "Free Vibration Study of Multilayer Sandwich Spherical Shell Panels With Viscoelastic Core and Isotropic/laminated Face Layers," Composites Part B: Eng., 159, pp. 72–85.
- [33] Permoon, M., Shakouri, M., and Haddadpour, H., 2019, "Free Vibration Analysis of Sandwich Conical Shells With Fractional Viscoelastic Core," Composite Struct., 214, pp. 62–72.
- [34] Vieira, F. S., and Araújo, A. L., 2020, "Optimization and Modelling Methodologies for Electro-Viscoelastic Sandwich Design for Noise Reduction," Composite Struct., 235, p. 111778.
- [35] Gibson, R. F., 2016, Principles of Composite Material Mechanics, CRC press, Boca Raton, FL.
- [36] Maheri, M., 2011, "The Effect of Layup and Boundary Conditions on the Modal Damping of FRP Composite Panels," J. Compos. Mater., 45(13), pp. 1411–1422.
- [37] Javidan, M. M., and Kim, J., 2020, "Experimental and Numerical Sensitivity Assessment of Viscoelasticity for Polymer Composite Materials," Sci. Rep., 10(1), pp. 1–9.
- [38] Kumar, N., and Singh, S., 2010, "Experimental Study on Vibration and Damping of Curved Panel Treated With Constrained Viscoelastic Layer," Composite struct., 92(2), pp. 233–243.
- [39] Krushynska, A., Kouznetsova, V., and Geers, M., 2016, "Visco-Elastic Effects on Wave Dispersion in Three-Phase Acoustic Metamaterials," J. Mech. Phys. Solids., 96, pp. 29–47.
- [40] Pichard, H., and Torrent, D., 2016, "Dynamic Homogenization of Viscoelastic Phononic Metasolids," AIP Advances, 6(12), p. 121705.
- [41] Baz, A. M., 2019, Active and Passive Vibration Damping, John Wiley & Sons, New York.
- [42] Golla, D., and Hughes, P., 1985, "Dynamics of Viscoelastic Structures— A Time-Domain, Finite Element Formulation," J. Appl. Mech., 52(4), pp. 897–906.
- [43] Lesieutre, G., and Bianchini, E., 1995, "Time Domain Modeling of Linear Viscoelasticity Using Anelastic Displacement Fields," ASME J. Vib. Acoust., 117(4), pp. 424–430.
- [44] Wagner, N., and Adhikari, S., 2003, "Symmetric State-Space Method for a Class of Nonviscously Damped Systems," AIAA J., 41(5), pp. 951–956.
- [45] Adhikari, S., 2010, "A Reduced Second-Order Approach for Linear Viscoelastic Oscillators," ASME J. Appl. Mech., 77(4), p. 041003.
- [46] Biot, M. A., 1955, "Variational Principles in Irreversible Thermodynamics With Application to Viscoelasticity," Phys. Rev., 97(6), p. 1463.
- [47] McTavish, D., and Hughes, P., 1993, "Modeling of Linear Viscoelastic Space Structures," ASME J. Vib. Acoust., 115(1), pp. 103–110.
- [48] Lesieutre, G. A., and Mingori, D. L., 1990, "Finite Element Modeling of Frequency-Dependent Material Damping Using Augmenting Thermodynamic Fields," J. Guid., Control, Dyn., 13(6), pp. 1040–1050.
- [49] Chakraborty, A., Mahapatra, D. R., and Gopalakrishnan, S., 2002, "Finite Element Analysis of Free Vibration and Wave Propagation in Asymmetric Composite Beams With Structural Discontinuities," Composite Struct., 55(1), pp. 23–36.
- [50] Reddy, J. N., 2003, Mechanics of Laminated Composite Plates and Shells: Theory and Analysis, CRC Press, Boca Raton, FL